RUSSIAN JOURNAL of EARTH SCIENCES

THEORETICAL AND EXPERIMENTAL MODELING OF LOCAL SCALE CO_2 FLUSHING OF HYDROUS RHYOLITIC MAGMA

A. G. Simakin[*,1], **V. N. Devyatova**[1], **and A. A. Shiryaev**[2]

[1] Korzhinskii Institute of Experimental Mineralogy, Russian Academy of Sciences, Chernogolovka, Russia
[2] Frumkin Institute of Physical Chemistry and Electrochemistry, Russian Academy of Sciences, Moscow, Russia
[*] **Correspondence to:** A. G. Simakin, dev@iem.ac.ru.

Abstract: Flushing of hydrous silicic magmas with crustal carbonic fluid may be an important factor controlling the dynamics of rhyolitic eruptions. We present combined theoretical and experimental study of the interaction of carbonic fluid with a hydrous silicic melt. The process of diffusional equilibration of a CO_2 bubble with a silicic melt was simulated numerically in the spherical shell approximation. The rapid water transfer from the melt to the bubble is followed by a slower diffusion of CO_2 into the melt. The water distribution in the melt becomes almost uniform over a period proportional to the diffusional unit of time $0.14\tau_\mathrm{w}$, determined by the initial inter-bubble distance W equal the distance between neighbor bubbles centers and the water diffusion coefficient D_w in the melt ($\tau_\mathrm{w} = W^2/D_\mathrm{w}$), while the CO_2 distribution remains strongly contrasting and the melt remains undersaturated in CO_2. This process was modelled experimentally with a hydrous albite melt at $P = 200$ MPa and $T = 950$–1000 °C. In the first series of experiments at $T = 950$ °C, a glass powder was filled with pure CO_2 at the beginning of the experiment, forming numerous bubbles at the run temperature. Micro-FTIR measurements showed that after 40 minutes the water content in the melt decreased from 4.9 down to 1.8 wt. % with the maximum CO_2 content of 500 ppm (below saturation). After 4 hours, the crystallinity increased to 85%, and almost all of the fluid bubbles escaped. The second series of experiments CO_2 interacted with a 2 mm high column of hydrous albite melt. Diffusion profiles in the quenched glass were measured using EMPA (H_2O) and micro-FTIR (CO_2 and H_2O). The estimated diffusion coefficients in the melt for H_2O (1.1×10^{-6} cm^2/s) and CO_2 (1.5×10^{-7} cm^2/s) are consistent with published data. Scaling analysis predicts that in the nature, after the influx of CO_2 bubbles a few millimeters in size, the maximum dehydration of rhyolitic magma with viscosity near 10^5 Pa s without a significant increase in CO_2 content occurs after 1–30 days, i.e. a period compatible with the minimum duration of pre-eruption processes in the magma chamber.

Keywords: Carbon dioxide, explosive volcanic eruption, experiment in IHPV, diffusion of CO_2 and H_2O, magma flushing with CO_2.

Citation: Simakin, A. G., V. N. Devyatova, and A. A. Shiryaev (2023), Theoretical and Experimental Modeling of Local Scale CO_2 Flushing of Hydrous Rhyolitic Magma, *Russian Journal of Earth Sciences*, 23, ES6007, EDN: CTVIQU, https://doi.org/10.2205/2023es000871

RESEARCH ARTICLE

Received: 23 March 2023
Accepted: 21 September 2023
Published: 30 December 2023

Copyright: © 2023. The Authors. This article is an open access article distributed under the terms and conditions of the Creative Commons Attribution (CC BY) license (https://creativecommons.org/licenses/by/4.0/).

Introduction

Intra-chamber degassing caused by CO_2 flushing at a mid-crustal depth can be an essential factor determining the explosive style of mafic magmas eruption [*Dallai et al.*, 2011]. Using geochemical and petrological tools, it is possible to distinguish the invasion of CO_2 into the magma from the assimilation of carbonate, causing the CO_2 generation in near-surface conditions (depth 1–3 km) by the enrichment of melt with CaO [*Mollo et al.*, 2010]. While processes involving carbonic fluid at the mid-crustal depths can only be studied indirectly, a high flux of CO_2 of deep origin is measured at the surface in mantle plume settings (Yellowstone [*Lowenstern and Hurwitz*, 2008; *Werner and Brantley*, 2003], Iceland [*Barry et al.*, 2014], Canary Islands [*Longpré et al.*, 2017] and some subduction zones (Italy [*Frezzotti et al.*, 2010]. *Frezzotti and Touret* [2014] suggested that CO_2 can be formed in the upper mantle during decarbonization reactions and can be transported to the crust either by dissolution in the mafic magma or along with it via deep tectonic dislocations (shear zones). During the upward migration, this fluid may cross magma chambers. The interaction of the carbonic fluid and water-bearing magmas can be equally important for basaltic and silicic compositions [*Caricchi et al.*, 2018]. Upon interaction with CO_2, the water undesaturated melt reaches saturation with respect to the CO_2-H_2O composite fluid. In addition to simple recharging, intra-chamber vesiculation may be a factor increasing the magma pressure in the chamber to a level sufficient to cause failure of the chamber roof and onset of an explosive eruption. The carbonic fluid transfers heat and dissolved components, thereby affecting the heat budget of the magma and its composition [*Simakin and Ghassemi*, 2018].

Fluxing of silicic magma with CO_2 of deep crustal or mantle origin or released from underplating basalts can affect the style of the eruption, increasing explosiveness, similar to mafic volcanism [*Dallai et al.*, 2011]. Melt inclusions (MIs) in quartz provide a unique opportunity to obtain direct information about the fluid regime of silicic magma.

The climatic eruptions of Yellowstone have been studied in details and analyses of MIs without water loss or corrected on water loss are available [e.g., *Befus and Gardner*, 2016; *Myers et al.*, 2016] and presented in Figure 1. Points of H_2O and CO_2 content form subvertical arrays, starting from compositions poor in CO_2 and undersaturated with water, extended vertically to solubility isobars of 200–250 MPa The Lava Creek Tuffs MIs exhibits water content variation in the range 3–4 wt. % [*Befus and Gardner*, 2016], while the Huckleberry Ridge Tuff MIs have higher water concentrations of 4–5 wt. % [*Myers et al.*, 2016].

Usually, such subvertical trends are interpreted as a manifestation of degassing due to depressurization. Figure 1 shows the calculated sequences of compositions of melts formed at pressure drops from 200 to 5 MPa in closed and open system modes [*Newman and Lowenstern*, 2002]. The interaction of CO_2-enriched fluid with magma (or flushing) also leads to degassing or dehydration of the melt, increasing the volume of the fluid phase. Assuming local equilibrium, as in modeling a pressure drop-induced degassing path, melt compositions will follow a solubility isobar as shown by the thick grey line in Figure 1, with compositions directed towards increasing CO_2 content. The same line with compositions directed towards increasing water content will characterize the process of magma crystallization with exsolution of excess fluid [*Wallace et al.*, 1995]. These trends are far from those observed for the Yellowstone eruptions data.

The interaction of a water saturated high-silica rhyolite melt with a CO_2 bearing ($X_{CO_2} = 0.4$) fluid at $T = 800$ °C and $P = 100$ MPa was experimentally studied by *Yoshimura and Nakamura* [2010]. Under the experimental conditions, the used bubble-free water-saturated glass slab was highly viscous (10^5 Pa s) and was partially dehydrated from the entire surface. In three-hour experiments, the H_2O concentration became uniform within a 0.5 mm thick melt volume, while the CO_2 distribution was still far from saturation. Disequilibrium effects were also observed during vesiculation after decompression of a melt saturated with CO_2 and H_2O, caused by slower diffusion of CO_2. Delayed saturation of the melt with CO_2 after dehydration can cause the melt compositions to follow the trend shown by the solid purple line marked by the upward arrow in Figure 1. In their vertical parts, the trends of equilibrium decompression degassing and disequilibrium CO_2 flushing are quite similar, which, at least requires not to ignore the possibility of the later process. Additional information, such as the isotopic composition (δ^7Li, δ^{11}B, δ^{34}S) [*Gurenko*, 2021; *Neukampf et al.*, 2022; *Zelenski et al.*, 2022] which is affected by isotope fractionation during degassing, could potentially help in choosing between these alternative mechanisms.

The dehydration of magma caused by CO_2 flushing leads to an increase in the liquidus temperature of magmatic minerals. This effect causes crystallization at a significant rate, exceeding the rate of quasi-equilibrium crystallization, due to the slow cooling of large volumes of magma beyond the reach of the geothermal circulation. Decompression degassing

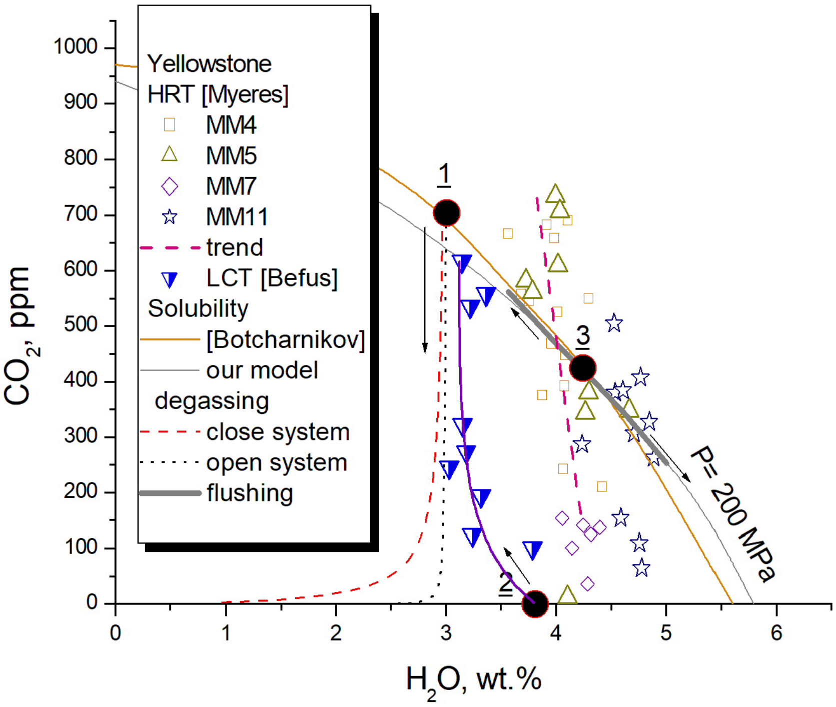

Figure 1. Compositions of melt inclusions in quartz from climatic eruptions of Yellowstone: Huckleberry Ridge Tuff (HRT), numbering of the different levels in the ash pile and analysis results from [*Myers et al.*, 2016], Lava Creek Tuff (LCT) data from [*Befus and Gardner*, 2016]. The decompression degassing lines (open and close system modes are depicted by dotted and dashed lines, respectively) were calculated and marked with an arrow pointing down. The line of flushing with CO_2 enriched fluid is shown as a solid line marked with an upward arrow, schematically. Evolution of the melt composition in equilibrium at flushing (marked with arrow directed towards increasing CO_2 content) and crystallization (marked with arrow directed to increasing H_2O content) is plotted with thick grey line as part of solubility isobar at $P = 200\,\text{MPa}$. Ideal compositions of the starting melt are marked with solid circles (1 – decompression degassing, 2 – dynamic flushing, 3 – equilibrium flushing or fluid exsolution at crystallization).

produces a similar effect of magma crystallization with an increase in undercooling, which has been well studied experimentally [*Cichy et al.*, 2010; *Couch*, 2003; *Simakin et al.*, 1999].

Here we present the results of the experiments in an internally heated high pressure vessel (IHPV) on the interaction of CO_2 with a hydrous albite melt, extending the results obtained by *Yoshimura and Nakamura* [2010]. Our experiments include studying the effect of albite crystallization caused by dehydration of the melt with CO_2 fluid. The results of numerical modeling of the growth of CO_2 bubbles during melt dehydration are also presented, which allow us to extend the experimental results to natural conditions with larger bubbles and a low fluid volume content.

Part 1. Numerical Modeling of Hydrous Melt Flushing with CO_2 on a Single Bubble Level

The Model

The interaction of a CO_2-enriched fluid with a hydrous melt (flushing) can be easily modelled theoretically in the equilibrium approach, similarly to the degassing process of a magma saturated with a two-component fluid. It is sufficient to know the mutual solubility of CO_2 and H_2O in a melt of given composition. An explosive eruption can start at a high rate on a time scale of hours or days. In this case, slow process of diffusive bubble growth can control compositions of the fluid and the adjacent melt. There are many approximate analytical and fully numerical solutions for diffusive equilibration (growth or dissolution) of a bubble in a melt [e.g., *Navon et al.*, 1998]. For clarity and consistency of consideration, we briefly describe the problem and methods of its solution.

Let us start with an analysis of the complete equation of diffusive mass transfer around a bubble growing in an infinite volume of the melt. The growing bubble expands and causes a radial flow of the melt with a rate (for the spherically symmetric case) $U(r)$. Therefore, the diffusion equation for any component of the melt can be written as:

$$\frac{\partial C}{\partial t} = -U(r)\frac{\partial C}{\partial r} + \frac{1}{r^2}\left(\partial\Big(D(C)r^2(\partial C/\partial r)\Big)/\partial r\right), \tag{1}$$

where $D(C)$ is the diffusion coefficient. The radial flow rate $U(r)$ is given by:

$$U(r) = \frac{U_0 r_0^2(t)}{r^2}$$

here $r_0(t)$ is the bubble radius at the moment t (see Table 1 for all physical parameters).

A set of bubbles of the equal size is usually [e.g., *Coumans et al.*, 2020] modeled in a spherical melt shell geometry. In this approximation, both the inner and outer (midpoint between neighboring bubbles) boundaries move as the bubble expands. The bubble growth rate is controlled by the diffusive flux of main component:

$$U_0 = \rho_\mathrm{m}/\rho_\mathrm{fl} D_\mathrm{w} \left.\frac{\partial C(r,t)}{\partial r}\right]_{r=r_0(t)+0}. \tag{2}$$

The influence of the flow is defined by the parameter $R_\rho = \Delta C \rho_\mathrm{m}$, where ΔC is the characteristic concentration difference $\Delta C = C_{r=r_0} - C_0$ (e.g., 0.01). It can be shown that for moderate values of $R_\rho < 1$ (pressures >100 MPa), the advection term can be omitted. At low pressures and fluid density, the parameter $R_\rho \gg 1$, and advection strongly affects the concentration field and transforms the solution to the type of a narrow boundary layer [*Zelenski et al.*, 2021]. Here we consider processes of the melt-fluid exchange in the magma chamber at a typical depth of about 7 km ($P = 200$ MPa) with $R_\rho \approx 0.1$ with a weak effect of advection. Our fluid consists of two main components CO_2 and H_2O, so two diffusive mass fluxes act on the bubble volume and the boundary condition (2) is replaced by:

$$\frac{\mathrm{d}V_\mathrm{bub}}{\mathrm{d}t} = \frac{\mathrm{dm}_{CO_2}/\mathrm{d}t + \mathrm{dm}_{H_2O}/\mathrm{d}t}{\rho_\mathrm{fl}(X)} + \frac{\mathrm{d}\rho_\mathrm{fl}/\mathrm{d}t}{\rho_\mathrm{fl}^2}\left(\Big(1 - X_{CO_2}\Big)\frac{\mathrm{dm}_{CO_2}}{\mathrm{d}t} - X_{CO_2}\frac{\mathrm{dm}_{H_2O}}{\mathrm{d}t}\right), \tag{3}$$

where m_{CO_2} and m_{H_2O} are the masses of the components in the bubble, X_{CO_2} is the mole fraction of CO_2 in the fluid, ρ_fl is the fluid density depending on its composition at fixed P and T. The concentrations of H_2O and CO_2 in the melt at the bubble boundary are assumed to be in equilibrium with the fluid composition:

$$C_{i,\mathrm{m}}(r = r_0) = F_i(X_{CO_2}),$$

where $i = CO_2, H_2O$, while at the outer shell boundary zero flux condition is applied

$$\frac{\partial C_{i,m}(r = r_1 - 0)}{\partial r} = 0.$$

Material Parameters.

Diffusion coefficients for CO_2 and H_2O in the melt are taken from [*Zhang and Ni*, 2010]. At $T = 850$–1000 °C, $P = 200$ MPa and $C_\mathrm{w} = 4$–5 wt. % the ratio D_{H_2O}/D_{CO_2} is in the range 4–10.

Table 1. Physical parameters

Variable	Dimension	Value	Name
C_i	wt %, ppm	CO_2 0–1000 ppm H_2O 0–5 wt. %	concentration in the melt
P	MPa	200	pressure
D_i	m^2/s	$H_2O \approx 10^{-10}$ $CO_2 \approx 10^{-11}$	diffusion coefficient in the melt
D_x	–	4–10	diffusivities ratio ($D_x = D_{H_2O}/D_{CO_2}$)
ρ_i	kg/m^3	fl ≈500 – fluid m ≈2300 – melt	density
R_ρ	–	0.16	effective density ratio ($R_\rho = \Delta C \rho_m/\rho_{fl}$)
R_0	m	10×10^{-6}– 2000×10^{-6}	bubble radius
R_1	m	–	outer radius of the melt shell
R, r	m	–	radial coordinate
$\xi = r/r_0$	–	–	dimensionless radial coordinate ($\xi = r/r_0$)
W	m	–	model inter-bubble distance ($W = 2R_1$)
τ_w	sec	–	water diffusional unit of time ($\tau_w = W^2/D_w$)
η	Pa s	$\approx 10^5$	viscosity of the melt
$\varepsilon, \varepsilon_{fl}$	–	0–0.4	bubbles volume fraction
ε_s	–	0–0.8	crystals volume fraction
τ_H	sec	–	water homogenization time ($\tau_H = 0.55\tau_w \varepsilon_{fl}^{2/3}$)
$U(r)$	m/s	–	radial flow rate in the melt shell around bubble
U_{st}	m/s	–	Stokes rate of bubble ($U_{st} = 1/3(\rho_m - \rho_{fl})gR_{0}2/\eta$)
τ_{st}	sec	–	Stokes time scale ($\tau_{st} = 1/U_{st}$)

The $CO_2 - H_2O$ fluid density was calculated from the model from [*Kerrick and Jacobs*, 1981]. We approximated $\rho_{fl}(X_{CO_2})$ and $d\rho_{fl}(X_{CO_2})/dX_{CO_2}$ for $T = 850\,°C$ and $P = 200\,MPa$ by a second order polynomials.

The solubility of H_2O (C in wt. %, P in kbar) was approximated as:

$$C_{H_2O} = 4.1(P(1 - X_{CO_2})^{1.35})^{1/2}$$

and CO_2 (C in wt. %, T in °C):

$$C_{CO_2} = 0.0592kX_{CO_2}^{0.79}, \; k = -0.54013 + 0.00164T,$$

where X_{CO_2} is the mole fraction of CO_2 in the fluid. These approximations correspond to experimental data for pressures $75\,MPa < P < 500\,MPa$, generalized for rhyolite in [*Botcharnikov et al.*, 2005], that can be illustrated by proximity of the model and experimental solubility curves in Figure 1.

Method of Solution.

For the numerical solution for the radial distributions of H_2O and CO_2 we apply the Lagrange formulation for spatial dimension, i.e. each node moves at the melt velocity [*Zelenski et al.*, 2021]. This approach was used in [*Lyakhovsky et al.*, 1996] to model bubble growth in the melt, it allows to drop advection term in (1) and avoid boundary conditions on the moving boundaries of the bubble. In Lagrangian formulation boundary conditions are set at the start and end points of the grid. In addition, for simplicity, we used the approximation of a constant diffusion coefficient at an average concentration C^*:

$$\frac{DC}{Dt} = D(C^*)\left(\frac{2\partial C/\partial r}{r} + \frac{\partial^2 C}{\partial r^2}\right), \tag{4}$$

where the Lagrangian total derivative D is applied on LHS of equation (4). The equation (4) was transformed to a dimensionless form by applying a linear scale equal to the initial bubble radius R_0 and a time scale t_0 related to the diffusion coefficient of water $t_0 = R_0^2/D_{H_2O}(C^*)$. Thus, the problem under consideration is characterized by two dimensionless parameters: R_ρ (see above) and $D_x = D_{H_2O}/D_{CO_2}$. Then Eqn. (4) was discretized using the global inverse square approximation [*Cheng et al.*, 2003]. Since the flow is weak, the nodes experience small displacements, and no new nodes were generated during the computations, as in the case of large R_ρ. Details of the algorithm first used to simulate superfast bubble growth in a lava flow are presented in [*Zelenski et al.*, 2021] and in a supplementary file to this publication. The best way to solve the complete nonlinear diffusion equation (1) is to use the control volume method [*Zelenski et al.*, 2021] However, the influence of an unexpected physical factor described in the experimental section below gives the nature of a preliminary analysis to our calculations.

Results

Our goal was to simulate the initial stage of interaction, when the process of transition of water from the melt to the bubble dominates. At a sufficiently long time, CO_2 migrates into the melt, and the molar fraction of CO_2 in the fluid decreases, so that part of the water returns to the melt. The increase in the volume of bubbles reaches a maximum at an early stage of dehydration of the melt. Here, we have estimated the minimum time required to obtain an almost uniform distribution of water in the melt around the bubble. The calculations are carried out at $D_x = 6$ (average value), $R_\rho = 0.046$ (corresponds to $\rho_m = 2.3\,g/cm^3$, $\rho_{fl} = 0.5\,g/cm^3$, $\Delta C = 0.01$) and several initial volume fractions of bubbles $\varepsilon_0 = (R_0/R_1)^3 = 0.005; 0.033; 0.053$. The time-successive radial profiles of water concentration in the melt at $\varepsilon = 0.033$ are shown in Figure 2a, 2b. Water migrates into the bubble, so its concentration in the melt decreases from 5 wt. % to 4.3 wt. %. A steep gradient of water concentration at $\tau = 0.5$ evolves almost to a flat one at $\tau = 5$. At the same time, CO_2 migrates into the melt. The concentration gradient is still steep at $\tau = 5$. In Figure 3, the distributions $CO_2(r)$ and $H_2O(r)$ are shown on the $CO_2(H_2O)$ plot. In this diagram, the distributions evolve from a steep concave curve to an almost vertical line ($\tau > 3$–4). With an order of magnitude decrease in the volume fraction of bubbles, the time of homogenization of the water content increases by ${\varepsilon_0}^{2/3}$ times, which is expected from the scaling relations. Figure 3 shows that the CO_2 content in the fluid, reflected by the maximum CO_2 content in the melt, increases with the volume fraction of the bubbles.

At short times, when the diffusion front is far from the outer boundary, the radial distribution of the ith volatile component can be described by a simple analytical solution in dimensionless coordinates $\xi = r/r_0$, $\tau = tD_i/r_0^2$. Here, we neglect the change in the boundary concentration, which depends on the composition of the fluid, and advection:

$$C(r,t) = c_0 + \frac{\Delta C}{\xi}\operatorname{erfc}\left(\frac{\xi - 1}{2\sqrt{\tau}}\right). \tag{5}$$

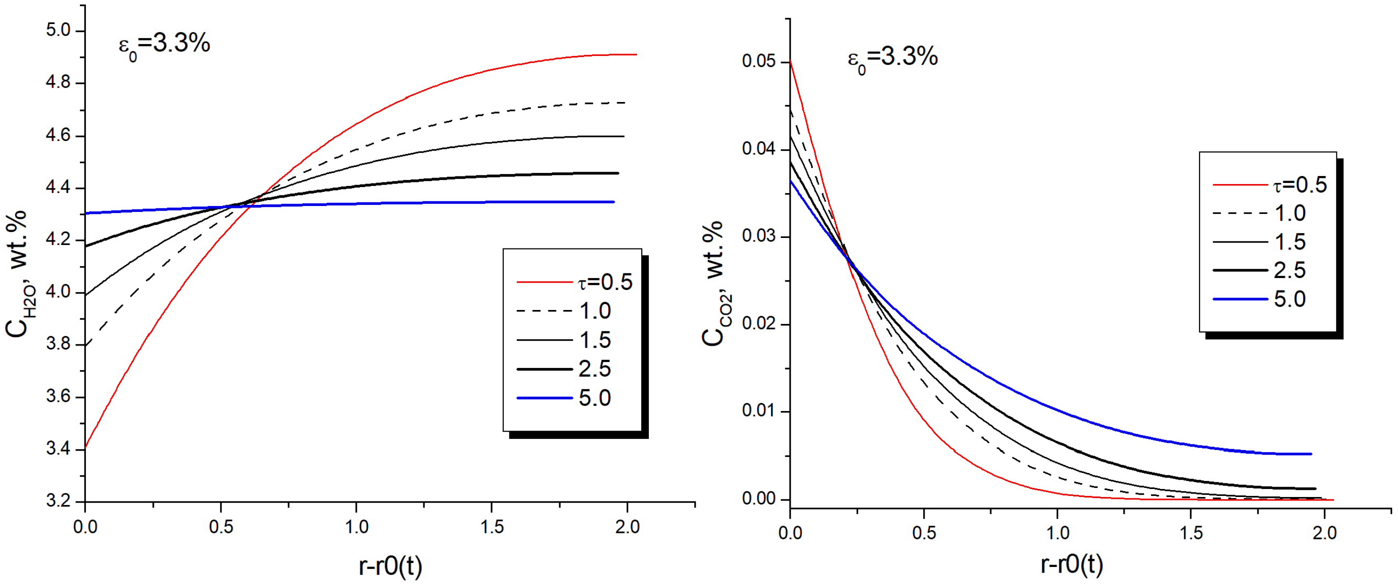

(a) (b)

Figure 2. Concentrations of CO_2 and H_2O in the melt at the contact with the a CO_2 bubble in the hydrous melt calculated at different moments of time (see legend). The distance from the contact is normalized to the initial bubble radius R_0, the time is scaled to the water diffusion time $\tau_0 = R_0^2/D_{H_2O}$, the initial water content is set at 3.3 wt. %. The linear dimensions of the bubble and melt shell correspond to the initial volumetric content of CO_2 fluid of 5 vol. %. See text for details.

Obviously, at $\tau \to \infty(\mathrm{erfc}(0) = 1)$ the distribution described by Eqn. (5) becomes a widely used stationary function $C(r,t) = \Delta C r_0/r$. Formally, the Eqn. (5) is a solution of the diffusion equation with an initial stepwise distribution: $C(r > r_0, 0) = c_0$; $C(r = r_0, 0) = \Delta C + c_0$. However, the solutions of the diffusion equation weakly depend on the initial conditions. In particular, if the boundary condition in time-dependent ($\Delta C = \Delta C(t)$), the distribution $C(r,t)$ is approximated by Eqn. (5) at a sufficiently slow change in the concentration at the boundary. As can be seen in Figure 3, the numerical and simplified theoretical dependences of $CO_2(H_2O)$ for a dimensionless time of 0.5 are quite close, which confirms the possibility of simple calculation of this dependence for various diffusion coefficients.

The ideal case of fluid exchange considered above may be far from those observed in nature, where the interaction of unevenly distributed moving bubbles with a fluid enriched in CO_2 and a hydrous melt occurs along with crystallization caused by dehydration. In the second part of the article, we report experimental results on CO_2 dehydration of albite melt, often taken as a model of silicic magmas, and consider these effects.

Part 2. Experimental Modeling of Crystallization Induced by CO_2 Flushing

Process of the bubble-magma interaction modelled above is only possible for a superheated magma. The interaction of hydrous albite melt at high temperatures with CO_2 generated *in situ* by interaction with calcite, was studied experimentally in [*Simakin et al.*, 2012]. The water content drops by 2 wt. % in several hours of flushing with CO_2 bubbles. Convection of albite melt at the millimeter scale caused by bubbles was observed. Natural melts are usually in equilibrium with one or more crystalline phases. The extraction of water by CO_2-rich bubbles induces their crystallization, since the loss of water increases the liquidus temperatures of magmatic minerals. The crystallization complicates simple process of diffusive fluid-magma interaction. We model this process in a simple albite – H_2O system at near liquidus temperature. In one series of the experiments, CO_2 bubbles with a characteristic inter-bubble distance of several tens of microns interacted with a hydrous albite melt. In the second series, the volume of albite melt interacted with the carbonic fluid via the upper interface to model the process on a larger linear scale of several millimeters.

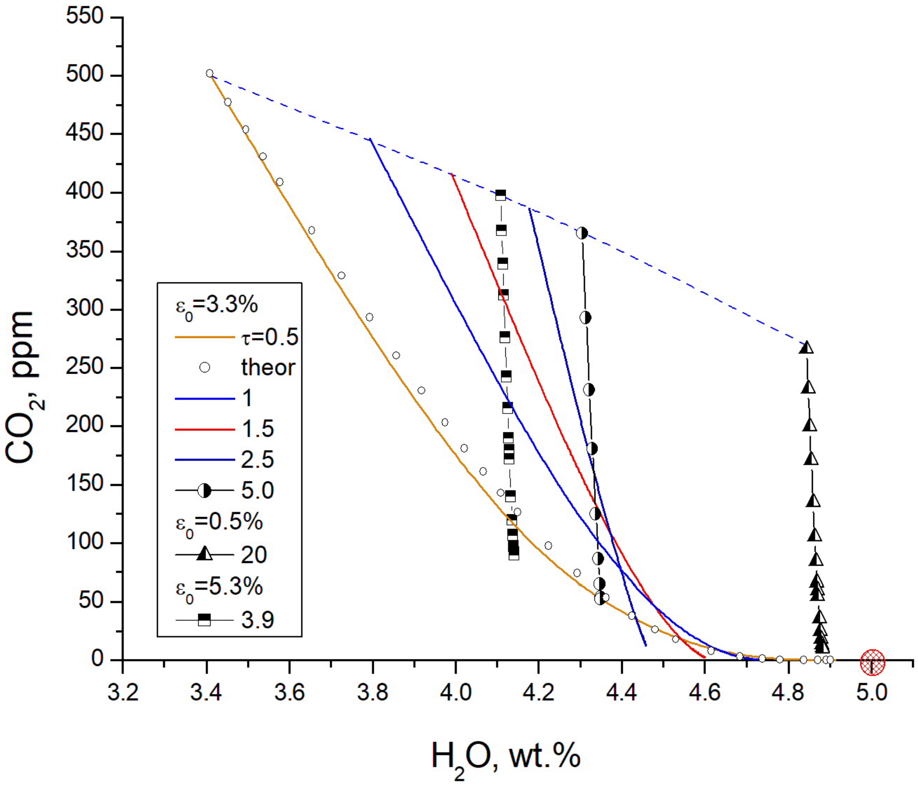

Figure 3. Calculated profiles C(R) of CO_2 and H_2O concentrations in the melt at the contact with the CO_2 bubble projected on the H_2O-CO_2 plot. The time intervals are shown in the legend (see Figure 1 for time scaling). The distributions are calculated for three volume fractions of the bubbles. The final distributions (symbols) of water and of CO_2 are, respectively, almost uniform and highly uneven. The points with the highest CO_2 content are on the fluid saturation curve (dotted line) and correspond to the fluid-melt contact. Theoretical values for the volume fraction $\varepsilon_0 = 0.033$ and dimensionless time $\tau = 0.5$ are calculated using eqn.(5). It takes more time to achieve a uniform distribution of water with a lower volume fraction of bubbles. The initial melt composition is shown by a hatched circle.

Experimental Technique and Methods

The experiments employing double capsule technique were carried out in Pt-capsules at IHPV (UHPG-10000 type) at IEM RAS and were terminated by isobaric quenching at a rate of 100–250 °C/min, and at 60 °C/s in some runs. The starting hydrous albite glass was produced from crystalline albite (natural mineral from Kalba, Kazakhstan) at $T = 1200$ °C and $P = 200$ MPa for 5 hours with the addition of a desired water content. To homogenize the water distribution, the glass was powdered and remelted at the same parameters. According to the Karl Fisher titration (KFT) data, the water content in the starting albite glass was 4.9 ± 0.1 and 5.1 ± 0.1 wt.% in the two series of experiments. Determination of the water content in the first glass by FTIR method gives a slightly lower value of 4.7 ± 0.1 wt.%.

In the first series of experiments, albite glass was a 100–200 µm powder, obtained by sieving and placed in a larger capsule. AgC_2O_4 loaded into a smaller capsule was used as a source of CO_2, in an amount providing a glass/CO_2 weight ratio of ~ 5. The small capsule (3 mm diameter) with the squeezed open end was placed in a large one (5 mm diameter), which was welded.

In the second series of experiments, glass cylinders were tightly inserted into the small capsules. The source of CO_2 was a mixture of $CaCO_3$ and quartz in an amount providing a glass/CO_2 weight ratio of ~ 1/2.5. To accelerate the decarbonization reaction with the formation of CO_2, a small amount of Na_2CO_3 or K_2CO_3 was added. The mixture was loaded into a large open capsule and covered with a separating platinum cap. Then a small capsule with a piece of glass was placed on the lid and the large capsule was welded. While using the cylindrical pieces of aluminosilicate glass, the fluid interacted with a melt through a sharp interface. Taking into account the curvature of the interface due to the capillary effect, this setting approximates a bubble in the melt with a size of several millimeters, which is consistent with real magmatic systems. On the contrary, in runs with the starting glass powder, due to the large number of bubbles, the reactions are complete in a short time. The experimental conditions, including temperature and duration, are shown in the Table 2 and 3.

Table 2. Series 1 of experiments with glass powder

a) Experimental data

#	time, min	$\varepsilon_{\mathrm{fl1}}$,%	$\varepsilon_{\mathrm{fl2}}$	ε_{s}, %	$C_{\mathrm{w,\,gl+s}}$ (EMPA)	$C_{\mathrm{w,\,gl}}$*	$C_{\mathrm{w,\,max}}$ (T_{run})
A21	40	9.9	3.5	8–10	2.5 ± 0.4	2.7	3.5
A20	75	7.0	2.6	10–13	2.7 ± 0.2	3.1	
A17	204	5.5	1.2	18–33	2.7 ± 0.7	3.6	
A15	242	0.7	0.1	64–76	2.5 ± 0.4	–	

Initial water content 5.1 wt. %, $T_{\mathrm{run}} = 950\,°\mathrm{C}$. $P = 200\,\mathrm{MPa}$.

*$C_{\mathrm{w,\,gl}}$ is an estimate of water content in the interstitial glass equal to $C_{\mathrm{w,\,gl+s}}/(1-\varepsilon_{\mathrm{s}})$ (average values of parameters are used), $C_{\mathrm{w,\,max}}$ (T_{run}) is liquidus water content at the run temperature, which is upper limit of $C_{\mathrm{w,\,gl}}$

b) Thermodynamic constrains on the equilibrium compositions of melt and fluid

#	almost complete crystallization			no crystallization	
	fluid – $X_{\mathrm{CO_2,\,min}}$	melt – $C_{\mathrm{w,\,eq}}$	$T_{\mathrm{m}}(C_{\mathrm{w,\,eq}})$, °C	fluid – $X_{\mathrm{CO_2,\,max}}$	melt – $C_{\mathrm{w,\,eq}}$
A21	0.66	2.80	1008	0.77	2.15
A20	0.67	2.74	1011	0.78	2.11
A17	0.70	2.57	1021	0.79	2.00
A15	0.71	2.51	1024	0.80	1.96

$X_{\mathrm{CO_2,\,min}}$ is minimal CO_2 mole fraction when practically all water is exsolved and $C_{\mathrm{w,\,eq}}$ is water content in the last residual melt, $T_{\mathrm{m}}(C_{\mathrm{w,\,eq}}) > T_{\mathrm{run}}$ is liquidus temperature of albite melt at $C_{\mathrm{w,\,eq}}$; $X_{\mathrm{CO_2,\,max}}$ fluid composition equilibrated with metastable albite melt with water content $C_{\mathrm{w,\,eq}}$.

Table 3. Series 2 of experiments with single glass piece

Experimental data					Thermodynamic estimates			
#	time,min	T_{run},°C	$C_{\mathrm{w,0}}$*, wt. %		$C_{\mathrm{w,max}}$ (T_{run})	almost complete crystallization		
			EMPA	IR		fluid – $x_{\mathrm{CO_2,min}}$	melt – $C_{\mathrm{w,\,eq}}$	$T_{\mathrm{m}}(C_{\mathrm{w,eq}})$, °C
A57	53	1020	2.0	2.2	2.43	0.97	0.2	1149
A63	108	1020	1.8	2.0 (1.7)	2.43	0.98		
A67	239	975	2.0 ± 0.1	–	3.09	0.98		

Initial water content 4.9 wt. %, $P = 200\,\mathrm{MPa}$,

* $C_{\mathrm{w,0}}$ is water content in the melt on the boundary with fluid; other symbols as in Table 1.

Weighing was done in an AUW220D analytical balance (Japan), with a measurement accuracy of ±0.1 mg for the mass range used. The composition of the run products were studied by SEM-EDS on a Tescan VEGA II XMU electron scanning microscope equipped with EDX analyzer with a Si(Li) INCA Energy 450 solid-state detector. The analysis was performed at an accelerating voltage of 20 kV. The obtained data were processed using the INCA Suite ver. 4.15 software with subsequent recalculation of the obtained results for weight contents using software packages developed by A. N. Nekrasov at IEM RAS. The Tescan Atlas program was used to process the BSE images and determine the phase proportions. The water content was analyzed using the Karl Fisher titration (KFT) on an AQUQ 40 device with a heating module for solids. According to the instrument calibration data, the accuracy of water determination is 3 rel. %. The Raman spectra of fluid from bubbles in experimental glasses were measured on a RM1000 spectrometer equipped with CCD detector, rejection filter, and Leica microscope. The spectra were excited using 532 nm solid-state diode laser. The laser beam was focused on a sample with 50× objective. The measurement parameters are as follows: laser power 22 mW, slit width 50 µm, and counting time 5×10 s.

The local content of water and CO_2 was measured on a Nicolet iN10 FTIR microscope equipped with a liquid nitrogen cooled MCT detector. The microscope and sample compartment were continuously purged with high purity dry nitrogen prior to and during the acquisition of the spectra. The measurements were performed in transmission mode at room temperature; the samples were carefully cleaned in acetone and placed on a KBr plate. The microscope was focused on the top surface of the sample. For the profiles, an aperture of $50 \times 50\,\mu m^2$ the measurement spots were immediately adjacent to each other. The spectra were obtained in the spectral range 600–6000 cm^{-1}. At least 64 scans were recorded per spectrum with a spectral resolution of 2 cm^{-1}. The FTIR spectra were processed using the Origin 9.5 software. Basic nonlinear correction was performed for each region of interest.

The interpretation of IR spectra requires additional information. Water contents were calculated from the combination 4500 cm^{-1} and 5200 cm^{-1} bands for hydroxyl and molecular water, respectively. The corresponding linear extinction coefficients and density of the albite glass were taken from [*Behrens et al.*, 1996] The signal of molecular CO_2 in IR spectrum at ~2349 cm^{-1} is superposed on a gaseous CO_2 doublet present as a trace despite the purging. The rotational bands of the dissolved CO_2 are suppressed. The spectral envelope was deconvoluted into three Gaussian components. After the deconvolution the contribution of atmospheric CO_2 peaked at 2336 and 2361 cm^{-1}. Carbon dissolved in the glass is also present as a carbonate ion. An isolated symmetrical ${CO_2}^{2-}$ ion has an active IR asymmetric stretching mode ν_3 at 1415 cm^{-1}. Adsorbed ${CO_3}^{2-}$ is characterized by the splitting of this band into two with a separation $\Delta\nu_3$, reflecting interaction with the substrate: weakly monodentate and strongly adsorbed bidentate ${CO_3}^{2-}$ ions are assigned to $\Delta\nu_3 = 100$ and 300 cm^{-1}, respectively [*Coenen et al.*, 2018]. In hydrous albite glass, one band at ≈1610 cm^{-1} overlaps with OH-bending mode of molecular water at ~1636 cm^{-1}. Subsequently, another band of the ${CO_3}^{2-}$ doublet at 1375 cm^{-1} was used in the analysis. The extinction coefficients for molecular CO_2 and ${CO_3}^{2-}$ were taken from [*Stolper et al.*, 1987]. CO_2 dissolves in albite melt mainly in the form of molecular CO_2. The fraction of the carbonate form increases with cooling and in quenched glass depends on the glass formation temperature T_g. [*King and Holloway*, 2002] used $r = CO_{2,mol}/(CO_{2,mol} + CO_{2,carb}) = 0.9$ in their analysis. Application of the thermodynamic model from [*Konschak and Keppler*, 2014] to our data at $T_g = 600\,°C$ gives $r = 0.73$. At low total carbon ($CO_{2,tot}$) the carbonate band at 1375 cm^{-1} is poorly resolved and the$CO_{2,tot}$ was estimated from data on molecular CO_2 corrected with $r = 0.8$ and 0.73.

Results of Experiments

The First Set of Experiments was performed at $P = 200$ MPa and $T = 950\,°C$. AgC_2O_4 used as the fluid source decomposes 100–200 °C below softening of the Ab glass. CO_2 fills the pores and forms bubbles when the glass powder melts. BSE and optic images showed that the bubbles are 50–200 µm in diameter with a population of tiny bubbles few microns in size. Volume fractions of both types of the bubbles are shown in Table 2 in columns $\varepsilon_{\text{fl}1}$ and $\varepsilon_{\text{fl}2}$, respectively. Over time, the bubbles quickly exsolved from the melt (see Table 2), assuring CO_2 flushing.

The local water content of the vesiculated glass was estimated using EMPA. The concentrations of all elements, including oxygen (with the exception of hydrogen), were measured by focusing the electron beam on a $10 \times 10\,\mu\text{m}^2$. This method reproduces well the KFT value of 5.1 ± 1.0 wt. % in the starting glass. Minimum water content drops to 2.5–2.6 wt. % in 30 min experiment (Table 1) and to 2.7–2.8 wt. % at 40 min duration. The Table 2 shows values corrected (divided on the glass volume fraction) for crystals present in the sampled areas. The minimum water content in the glass can be estimated based on the composition of the fluid (column $X_{CO_2,\min}$ in Table 2), assuming that all water has partitioned into the fluid. The values of $X_{CO_2,\min}$ in different runs differ slightly due to the variation in the mass ratio of the glass and $Ag_2C_2O_4$. During the crystallization of albite glass, the water content in the melt cannot exceed $C_{\text{w,max}} = 3.5$ wt. %, at which the run temperature $T = 950\,°\text{C}$ is equal to the melting temperature of albite at $P = 200\,\text{MPa}$ (calculated based on the data from [*Holland*, 2001]). All values of the water content estimated with EMPA are in the range $C_\text{w}(X_{CO_2,\min}) < C_\text{w} < C_{\text{w,max}}$, except for run a15. During the albite crystallization, water is released, which partially compensates its transfer to the CO_2-enriched fluid. Since the samples from the first set of experiments contain a large number of crystals and bubbles, it is difficult to use the micro-FTIR method to accurately analyze the H_2O and CO_2 content. Several measurements were performed only for glass a21 from a short run. IR spectroscopy gives a water content in the range 1.8–4.2 wt. %, which is consistent with the results of EMPA (see Table 2 and Figure 4). The lowest value of $C_\text{w} = 1.8$ wt. % corresponds to the equilibration of the water content with bulk interaction of the fluid with the melt without crystallization. In two analytical points, the content of water and carbon dioxide fall on the solubility curve within the measurement uncertainty. The melt at the other three points lost water but did not receive enough CO_2 to become saturated with fluid.

In the first series of experiments, the fluid composition in the bubbles was characterized by the Raman spectroscopy. CO_2 was identified by the characteristic Fermi dyad at 1385 and 1281 cm^{-1} (see Figure 5f). Density of the fluid (ρ_fl) in the bubbles was estimated from the difference of positions of these bands (the dyad splitting Δ, cm^{-1}). Since the spectral resolution of the Raman spectra is $1.5\,\text{cm}^{-1}$, exact positions of the bands maxima were determined from approximation of the peaks with a Lorentzian lineshape as recommended in [*Yamamoto and Kagi*, 2006]. The empirical relationship $\rho_{fl}(\Delta)$ from *Wang et al.* [2011] was used. The CO_2 density in the bubbles was evaluated in the samples a20 and a17, showing a rapid increase in the crystallization degree with an increase in the run duration from 75 to 204 minutes, respectively (see Table 2). The obtained values are $0.566 \pm 0.010\,\text{g/cm}^3$ ($n = 3$) and $0.673 \pm 0.006\,\text{g/cm}^3$ ($n = 3$) for a20 and a17, respectively. The CO_2 density in bubbles in the quenched glass carries information about composition (H_2O/CO_2 ratio) of the fluid at the parameters of the experiment; however, the interpretation of these data, complicated by numerous factors, is beyond the scope of our work.

In the shortest experiment (a21) the albite crystallization caused by dehydration was confined the former boundaries of glass powder chips (Figure 5a). These surfaces were exposed to CO_2 at the beginning of the experiment prior to the melting, and it is likely that microcrystals could have nucleated there and continued to grow at high temperature. The crystals possess a highly elongated morphology. The length of the crystals at 30 min is 15 µm, at 40 min – 24.3 µm. With an increase in the experiment duration to 2 hours, the crystallization degree reaches 80–85 vol. %. These observations correspond to the albite growth rate of about 1.3×10^{-8} m/s, which is almost two orders of magnitude higher than the growth rate of feldspar from rhyolite melt under similar conditions [*Rusiecka and Baker*, 2021; *Simakin and Chevychelov*, 1995], which is slowed by diffusion in the melt.

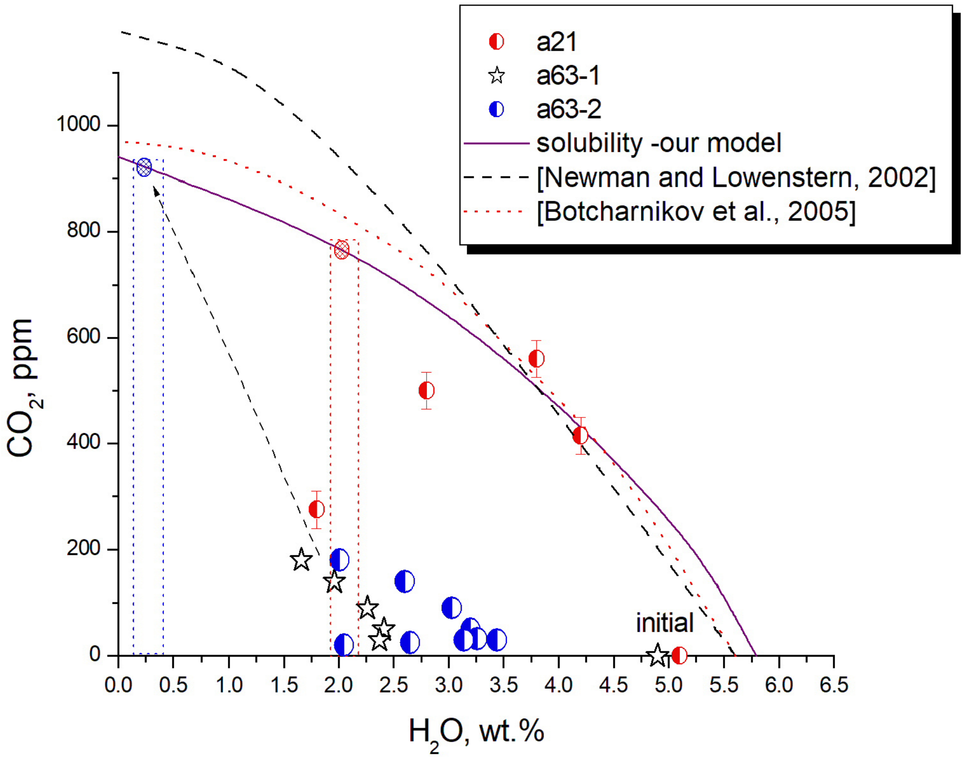

Figure 4. The results of our experiments on the composition of the fluid dissolved in the albite melt. Two profiles measured with µ-FTIR on two pieces of glass from the run a63 with frontal dehydration are represented with half-filled circles and open stars. Discreet points in the bubbly glass from the experiment a21 are marked with small red half-filled circles. The model solubility curve at 200 MPa and literature data are shown with lines. The equilibrium compositions for the exchange of the melt with CO_2 in the experiments are shown by hatched circles. The dotted boxes depict the expected locations of compositions homogenized with H_2O prior to homogenization with CO_2.

Homogeneous nucleation in albite melt is extremely difficult to achieve, making this composition ideal for glass formation [*Zanotto and Cassar*, 2017]. In our case, the glass powder with a high surface area interacted with CO_2 at temperatures below T_g, which led to the formation of numerous nucleation centers. Since the growth rate is high, the dehydrated albite glass crystallized efficiently. The volume fraction of crystals (ε_s) increases with time as indicated in Table 2 and shown in Figure 5a-d. The transformation kinetics can be approximated with Johnson – Mehl – Avrami – Kolmogorov (JMAK) equation $\varepsilon_s = 1 - a \cdot \exp(-(k \cdot t)^n)$ [e.g., *Yinnon and Uhlmann*, 1983]. The model with $n = 3$ and $a = 1$ characterizing the growth of crystals on preexisting nuclei formed on the surface of glass particles at low temperatures, does not fit the data (Figure 6). The proportion of solids extrapolated to the beginning of the experiment is non-zero (coefficient a less than 1). The best fit model has a value of $n = 10.5$, much larger than the maximum theoretical value of $n = 4$. This implies violation of the constant nucleation rate assumption underlying the JMAK equation. The extremely high rate of transformation in the time interval of 180–250 min may be associated with the rapid delayed homogeneous nucleation during this period. With more data available, the transformation kinetics can be approximated by a sum representing a set of nucleation events with different delay times [*Narine et al.*, 2006].

The Second Set of Experiments aimed to reproduce the scenario with a large inter-bubble distance and large bubbles. The carbonic fluid was in contact with a few mm thick volume

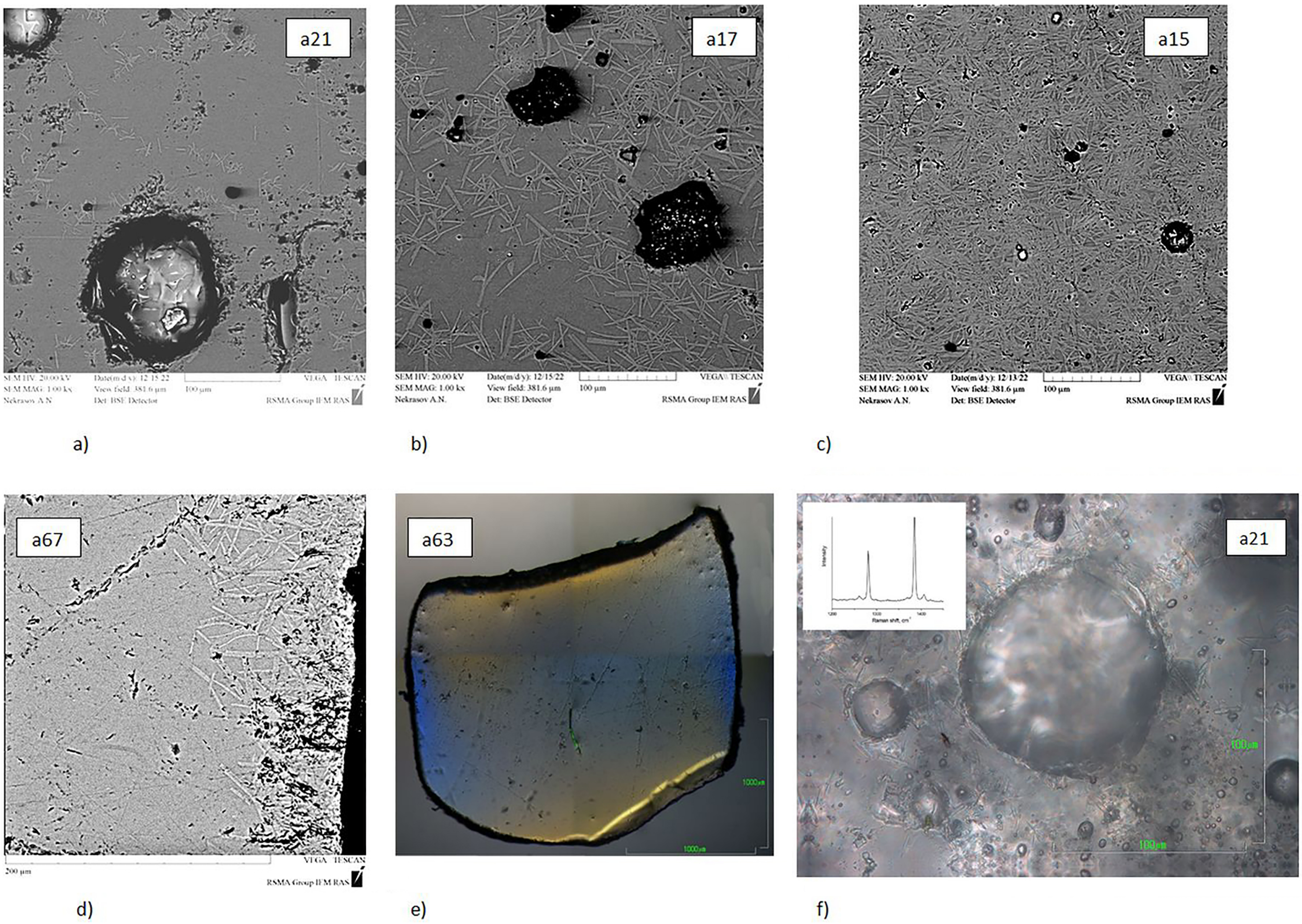

Figure 5. BSE (a–d) and optical (e,f) images of the experimental products, run numbers are indicated on the images. Images (a–c) show gradual increase in crystallinity and a decrease in the fluid bubbles fraction over time. d) In run a67 albite crystallization started from the capsule wall after dehydration of the melt near the contact. e) Double-polished glass plate used in µ-FTIR analysis. f) Optical image of the glass slice from run a21 (shortest duration 40 minutes) shows the presence of the small bubbles present in the starting imperfect glass, and larger bubbles rich in CO_2, reaching large size due to coalescence; Raman spectrum of CO_2 is in the inset.

of hydrous albite at the capsule bottom. At temperature $T = 1020\,°C$ an unexpected mechanism of the interaction between CO_2 and albite melt was observed. In a short experiment a57 (duration 53 min) the distribution of water was estimated using EMPA and is shown in Figure 7. The water concentration at the upper boundary of the profile was $C_w \approx 2$ wt. %. Since the starting glass for this experiment contains many microbubbles, only one measurement of the water content at the boundary was performed using µ-FTIR, which gives $C_w = 2.3$ wt. %. These values are much higher than $C_w \approx 0.2$ wt. %, corresponding to the equilibrium solubility in the fluid with $X_{CO_2} \geq 0.9$. More accurate data for both H_2O and CO_2 (Figure 8) were obtained using µ-FTIR for the run ab63 performed under the same PT conditions with bubble-free starting glass (see Table 3 and Figure 5e). The water contents at the boundary of 2.01 and 1.66 wt. % is close to 2–2.3 wt. % at the boundary in run a57 (Table 3). It is noteworthy that the CO_2 content near the contact is significantly smaller than the saturation level expected for a fluid with a high CO_2 mole fraction. As seen in Figure 4, the pair of concentrations (C_{H_2O}, C_{CO_2}) near the contact with the fluid for the run a63 does not approach the saturation curve for $P = 200$ MPa, in contrast to the data presented in [*Yoshimura and Nakamura*, 2010].

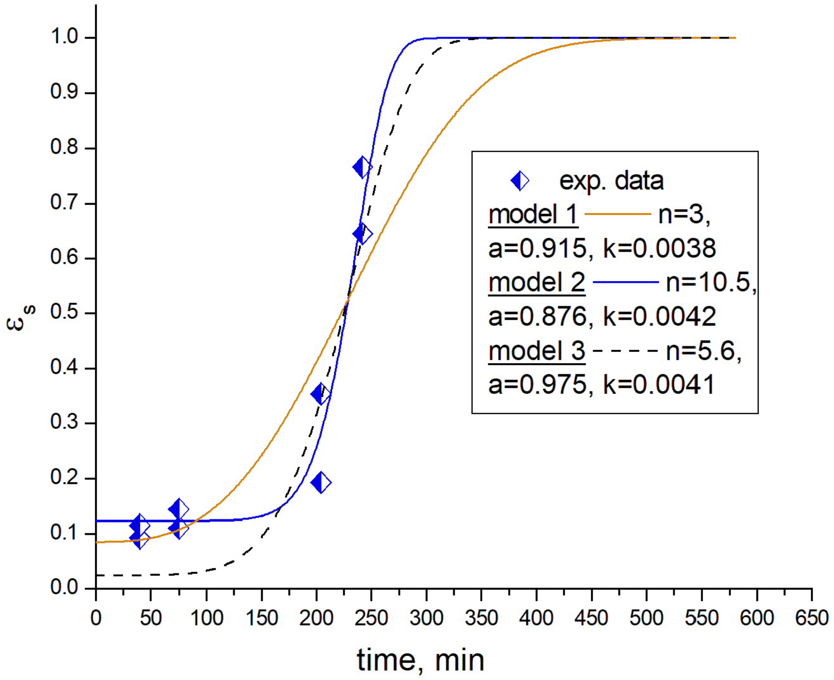

Figure 6. Time-dependence of the volume fraction of crystals in the bubble-free melt in the first series of experiments with starting albite glass powder. The experimental points (semi-filled diamonds) are approximated by the modified JMAK equation $\varepsilon_S = 1 - ae^{-kt^n}$ (see text) with the parameters indicated in the legend. The coefficient a is taken to be less than 1 to account for the rapid crystallization from the surface of glass fragments upon contact with CO_2 at the beginning of experiment. The classical model with $n = 3$, implying kinetic control without nucleation, poorly fits the observations. The preferred model 2 with $n \approx 10$ implies rapid homogeneous nucleation with large delay time.

Since there were no signs of crystallization visible on the SEM and optical images in the contact area, we assume that the dense CO_2 fluid interacted with the melt surface and extracted mainly Na and Al, enriching the upper melt film with silica. To explain the observations, the concentration gradients in this protective film must be very high, and the diffusion coefficients must be several orders of magnitude lower than in the albite melt. This hypothesis was tested using experimental data on the diffusion coefficients of CO_2 and H_2O in silica glass [*Behrens*, 2010]. It was found that a silica glass film about 2 µm thick will provide the concentrations and the diffusion fluxes observed on the melt surface in run a63.

Another unusual feature of the mechanism of interaction between albite melt and pure CO_2 at high temperatures is the decrease of the water content in the melt the near the capsule walls in the run 63. From the µ-FTIR data (Figure 8) it can be noted that the water content decreases towards the bottom and that the second, incomplete, profile is characterized by lower concentrations, since it was closer to the wall. At the same time, the CO_2 distributions follow the same dependence with a monotonously decreasing concentration with distance from the contact. These observations can only be explained by the action of some mechanism of ultrafast surface diffusion of water, but not of CO_2, along the Pt-melt interface. This mechanism equalizes the boundary concentration of water with values near the active upper contact with the fluid.

At a lower temperature of 975 °C (runs a67 and a68) crystallization began (Figure 5d) from the upper surface and, in some places, near the bottom of the capsule. In this case,

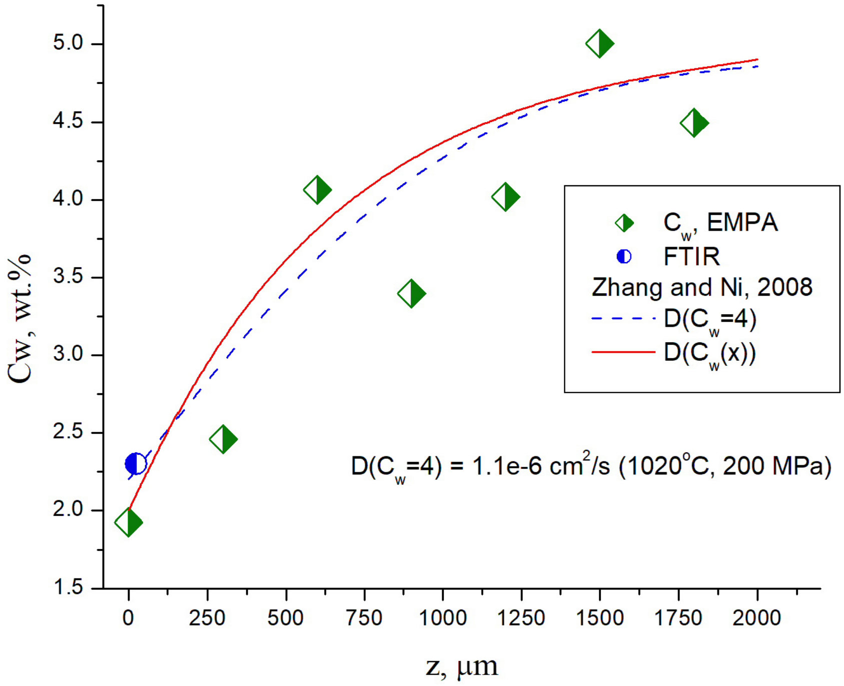

Figure 7. Water distribution in glass from experiment a57, demonstrating dehydration in contact with a CO_2-enriched fluid. Water concentrations were estimated with EMPA. Several theoretical profiles calculated with the parameters of the experiment a57 are shown; the diffusion profile at a constant boundary condition and diffusion coefficient calculated at a constant $C_W = 4$ wt. % is depicted by a dashed line; the profile shown in solid line is calculated with a diffusion coefficient dependent on water content [*Zhang and Ni*, 2010].

the concentration of water in the contact with the crystallization front was estimated only with EMPA at the level of 3.0 ± 0.5 wt. %, which is close to the water content of 3.1 wt. % in albite melt in equilibrium with crystalline albite under experimental PT conditions (see Table 3). The minimum growth rate of albite, calculated assuming zero nucleation delay time, is 0.9×10^{-8} m/s (run ab68-4) and 0.98×10^{-8} m/s (run ab67), which is somewhat lower than the estimate of 1.3×10^{-8} m/s obtained in the first series of experiments. It can be noted that the composition of alkali feldspars in the runs ab68 and ab67 slightly differ in potassium content with $K_2O = 0.35 \pm 0.10$ wt. % and 0.11 ± 0.10 wt. %, respectively. This difference is explained by the use of K_2CO_3 and Na_2CO_3 to stimulate the generation CO_2 in the reaction of $CaCO_3$ with SiO_2 in runs ab68 and ab67, respectively.

We model the distribution of water measured in run a57 by solving 1D diffusion equation with a variable diffusion coefficient:

$$\frac{\partial C(x,t)}{\partial t} = \frac{\partial D}{\partial C}\left(\frac{\partial C}{\partial x}\right)^2 + D\frac{\partial^2 C}{\partial x^2} \tag{6}$$

The diffusion front of dehydration in this run did not reach the lower boundary of the melt. Therefore, a constant water content of 4.9 wt. % at the bottom and 2 wt. % on the surface were taken as boundary conditions. The diffusion coefficient in silicic melts varies by about half an order of magnitude due to change in the water content, is a function of temperature, composition, and C_{H_2O} [*Zhang and Ni*, 2010]. Equation (6) was solved numerically using the built-in solver (FDM+Newton iterations) of the MAPLE 9.5 commercial software. EMPA measurements are relatively well reproduced both

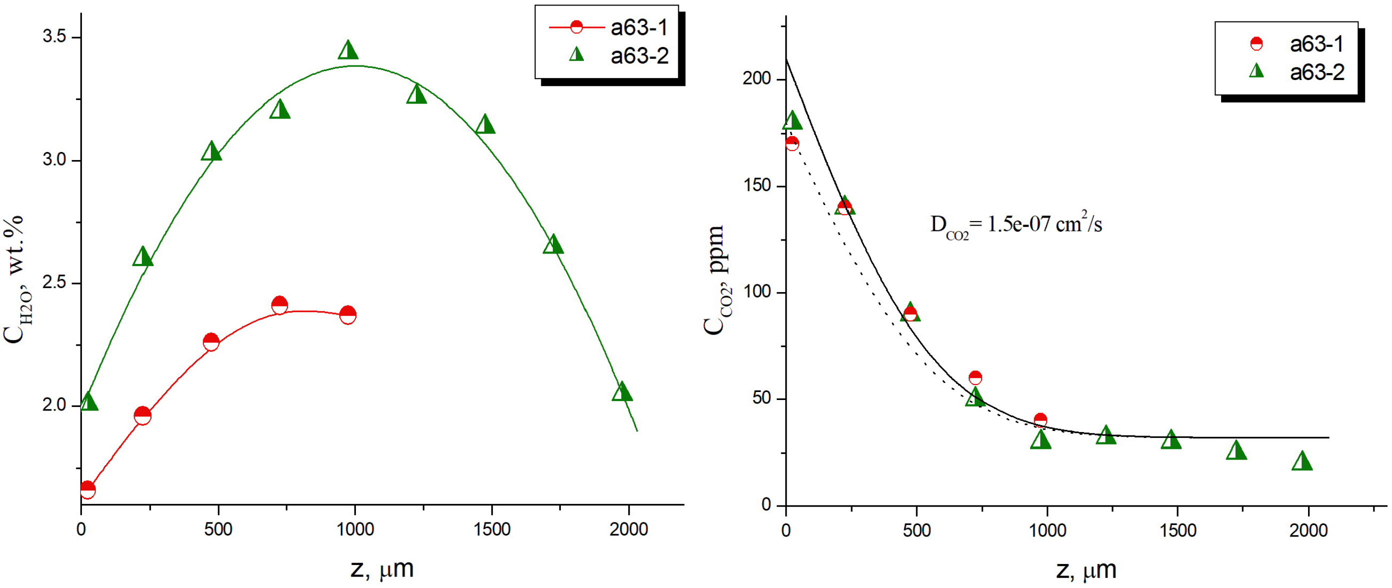

(a) **(b)**

Figure 8. The content of volatiles on two profiles across the glass from the run a63 from the top contact towards the bottom a) H_2O distributions for full (semi-filled triangles) and half (semi-filled circles) profiles b) CO_2 distributions and their approximation by a complementary error function (erfc), the value of the fitted diffusion coefficient is shown in the plot.

at concentration dependent and calculated at $C_\mathrm{w} = 4\,\mathrm{wt.\%}$ values of the diffusion coefficient (Figure 7). The distribution of water in the run a63 is three-dimensional due to the loss of water from the entire surface of the melt and a large diffusion time (dimensionless $\tau > 5$). For the run a63 only the CO_2 distribution was considered due to its 1D character since the influx of CO_2 occurs only from the upper contact of the fluid with the melt (Figure 8b). The CO_2 diffusion coefficient obtained by fitting with a complementary error function (erfc), is 1.5×10^{-7} cm^2/s, which is equal to the value calculated from the model from [*Zhang and Ni*, 2010] at $C_{\mathrm{H}_{20}} = 4\,\mathrm{wt.\%}$.

The distributions of water and carbon dioxide are projected onto the graph ($C_{\mathrm{H}_{20}}$, C_{CO_2}) in Figure 4. On this plot the studied case of extreme dehydration with pure CO_2 at a high mass ratio of CO_2/melt is characterized by a convex path that deviates significantly from the predicted series of concave trajectories evolving towards a vertical line (see Figure 3 and in [*Yoshimura and Nakamura*, 2010]. In our case, it should have a maximum CO_2 content approaching 1000 ppm and a H_2O concentration of less than 1 wt.%. As mentioned above, the influence of the protective film and ultrafast diffusion of H_2O along the Pt-melt interface leads to the observed CO_2(H_2O) trajectory configuration.

Application to Rhyolitic Magma

Scaling

Schematic diagram showing principle parameters of the CO_2 flushing process in our numerical modeling, experiments with albite melt and in natural environments with initial bubble radius R_0 and inter-bubble distance $W = 2R_1$ is shown in Figure 9. Several lines of constant initial volume fraction of fluid ε_fl are plotted on this figure to delineate the parametric area expected in nature, encountered in experiments with albite melt and used in numerical modeling. In the process of the water migration in the melt, the water diffusion time scale is $\tau_\mathrm{w} = R_0^2/D_\mathrm{w}$. As demonstrated above, homogenization of the melt in H_2O takes 4–20τ_w depending on the inter-bubble distance $W = 2R_1$ or equivalent bubbles volume fraction $0.005 < \varepsilon_\mathrm{fl} < 0.05$. Our modeling data correspond to a simple dependence for the homogenization time $\tau_\mathrm{H} = 0.55\tau_\mathrm{w}{\varepsilon_\mathrm{fl}}^{2/3}$. After substituting the expression for $\varepsilon_\mathrm{fl} = (R_0/R_1)^3 = 8(R_0/W)^3$ into the expression for τ_H, we get $\tau_\mathrm{H} = 0.138W^2/D_\mathrm{w}$. For experimental conditions water diffusion coefficient is calculated at the average C_w=1.5 and

4 wt. % and $T = 950\,°C$. In the first series of experiments with albite melt homogenization time τ_H is 3–9 minutes (see Figure 9). The residence time of bubbles in the melt in these experiments depends on their size, distance from the surface, and the local melt viscosity. The volume fraction of large bubbles rich in CO_2 over time is well described ($R^2 = 0.9995$) by the exponential function $\varepsilon_{fl} = 0.06 + 0.34\exp(-t/t_0)$ with $t_0 = 19$ minutes. This means that some bubbles may leave the melt before equilibration even in terms of water distribution. The duration of experiment a21 is comparable to the expected time of water homogenization. The duration of other experiments is several times longer, albite crystallization and diffusive migration of the exsolved water occurred on the scale of the entire sample with water loss through the surface.

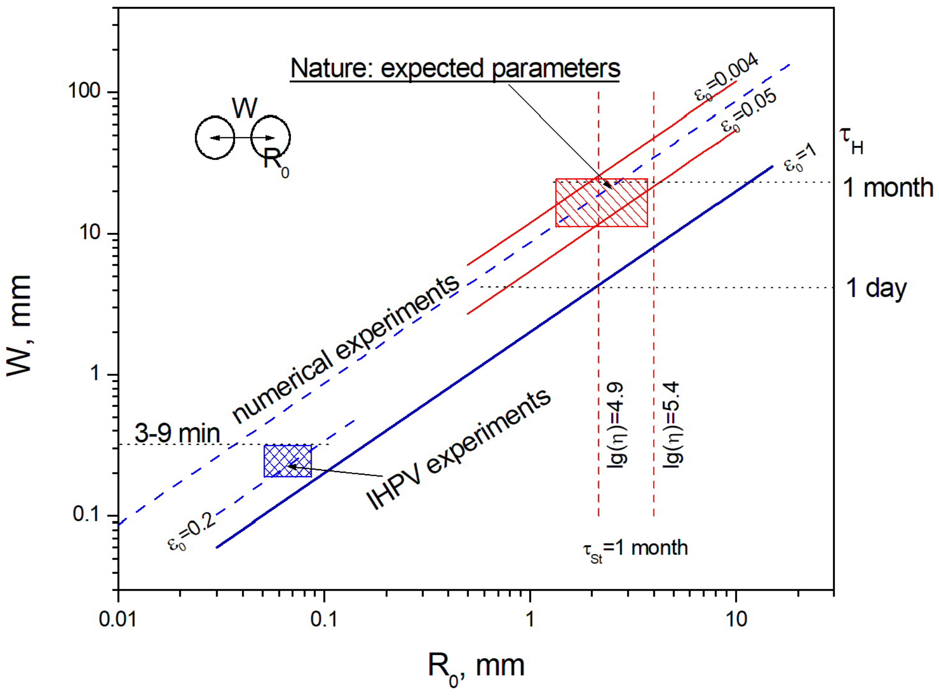

Figure 9. Schematic diagram showing the principle parameters of the CO_2 flushing process in our numerical modeling, experiments with albite melt and in nature. A homogeneous distribution of identical bubbles, the initial bubble radius R_0 and the inter-bubble distance W equal to $2R_1$ in the spherical shell model are assumed. The lines of the constant initial fraction of bubbles ε_0 are shown. The dashed lines show the average parameters of the numerical and IHPV experiments. Several values of water homogenization time $\tau_H = W^2/D_w$ are plotted near the vertical axis. For experiments with albite melt, the water diffusion coefficient D_w was calculated for $C_w = 1.5$ and 4 wt. % at $T = 950\,°C$, for natural rhyolite (τ_H values near the right axis) at $C_w = 4$ wt. % and $T = 800\,°C$. The vertical dashed lines correspond to the Stokes time $\tau_{st} = 1$ month (see text) calculated for the albite melt with $C_w = 4$ wt. % at $T = 800\,°C$ and rhyolite magma (larger values of viscosity and R_0) at the same parameters. For bubbles with $R_0 \le 1\,\mathrm{mm}\tau_{st} > \tau_H$ which means local equilibrium H_2O with melt and possible CO_2 unsaturation. In the experiments with albite melt, water and melt are expected to equilibrate on the scale $R_0 \approx 100\,\mu m$.

Upon reaching the homogenization of water in the melt at τ_H, dehydration reaches a maximum. Later, when CO_2 is equilibrated with the melt, the H_2O content increases to the equilibrium value following a decrease in the CO_2 concentration in the fluid. The bubbles volume also reached its maximum at τ_H. With a volume fraction of CO_2 from 0.4 vol. % to 4 vol. %, the proportion of CO_2 transferred into the melt is from approximately

0.4 to 0.06. Applying our results to nature, we can assume that after the bubbles of fluid enriched in CO_2 start at the bottom of the magma chamber, their residence time will depend on the dynamics of the magma The bubbles move relative to the melt at a rate close to the Stokes velocity (the rise of a single bubble in an infinite volume of liquid) $U_{\mathrm{st}} = 1/3(\rho_{\mathrm{m}} - \rho_{\mathrm{fl}})gR_0^2/\eta$. Obviously, this bubbles transfer mechanism can be only local at a time scale close to τ_{H}. However, the density of the fluid is much less than that of the melt, and the volume of bubbly magma will induce convective flow. For a single convective cell, the convection rate will be much higher than the Stokes rate. Using the results of [*Simakin et al.*, 1997], it can be shown that at $\varepsilon_0 = 0.2\,\mathrm{vol.\%}$ (regardless of phase densities and melt viscosity) the convection rate will be approximately equal $U_{\mathrm{conv}} = 0.6U_{\mathrm{st}}(H/R_0)$, where H is cell height and R is bubble radius. At $H = 100\,\mathrm{m}$ and $R_0 = 0.001\,\mathrm{m}$, the convection velocity will be approximately 6×10^4 times higher than Stokes rate. Then the minimum time for bubbles to escape from the magma due to Stokes flow τ_{st} becomes proportional to the ratio of the typical width of the convective boundary layer of 1 m [*Simakin and Bindeman*, 2022] to the Stokes bubble rise velocity U_{st}. Figure 9 shows the Stokes times equal to one month (vertical dashed lines) calculated for albite melt with $C_{\mathrm{w}} = 4\,\mathrm{wt.\%}$ at $T = 800\,°\mathrm{C}$ and rhyolitic magma (larger values of viscosity and R_0) with the same parameters with the model [*Hui and Zhang*, 2007]. For real values of R_0 and $\varepsilon_{\mathrm{fl}}\tau_{\mathrm{st}} > \tau_{\mathrm{H}}$, so we expect local homogenization of water concentration corresponding to local values of $\varepsilon_{\mathrm{fl}}$. Since diffusion of CO_2 is 6–10 times slower, the melt can be dehydrated, but not saturated with CO_2. Whatever the physical mechanism of bubble transport for sufficiently large bubbles in rhyolitic magma chambers, the local time of water homogenization becomes compatible with the typical time scale of pre-eruption processes, i.e. in the range of days and months.

Discussion

The unexpectedly low concentration of CO_2 and high concentration of H_2O at the contact between CO_2 and hydrous albite melt, observed in our experiments (Figure 7,8), measured with resolution of micro-FTIR method of about 50 µm and resolution of EMPA method of about 5 µm, we explained by the presence of ultrahigh concentration gradients in a narrow boundary layer, which we could not resolve. Under the PT conditions of run a63, the diffusion coefficient of H_2O decreases only by a factor of 5 when the water content in the albite melt decreases from 4 wt.% to zero [*Zhang and Ni*, 2010]. This means that the width of the diffusion zone in albite melt with a decrease in water concentration from 2 wt. % to zero should be only a few times narrower than when falling from 3.5 wt. % to 2 wt. % ($\approx 1000\,\mu\mathrm{m}$), and can be resolved using available analytical methods. The formation of a near-surface layer of a contrasting composition rich in SiO_2 with high viscosity and low diffusivities during the extraction of Na_2O and Al_2O_3 with CO_2 fluid can explain the observations. Direct experimental measurements of the solubility of the main and trace elements of the melt in supercritical CO_2 under high PT conditions have not been carried out. Observations of CO_2 fluid inclusions contained in pyroxenes indicate high solubility of Al_2O_3, Na_2O, K_2O, Rb_2O, SrO and other oxides at a pressure of about 1 GPa and a temperature of about 1000 °C [*Berkesi et al.*, 2012; *Hidas et al.*, 2010]. Our hypothesis is worth testing, since the likely effect of a protective film can significantly affect estimates of the rate of exchange of hydrous magma with pure CO_2 in nature.

The albite crystals grown in our experiments had a strongly elongated and sometimes even curved morphology (see Figure 5a–d), reflecting strong undercooling that occurs during melt dehydration. In nature, when the composition of the melt is in a quartz field, the formation of non-equilibrium morphologies of quartz crystals is expected in a dehydrated melt. As established experimentally, the transition from flat faceted to skeletal morphology of quartz occurs at $DT \approx 55\,°\mathrm{C}$ [*Swanson and Fenn*, 1986]. Quartz crystals from the large (climatic) explosive eruptions (LCT, Yellowstone; Toba Tuff, Indonesia; Oruanui Tuff, New Zealand) of rhyolitic magma have reentrants, i.e., deep glass embayments open towards the edge of the crystal [*Befus and Manga*, 2019; *Ruefer et al.*, 2021]. Their origin may be related to the non-equilibrium growth stage of quartz with skeletal morphology.

The experiments did not confirm the hypothesis that reentrants can be formed during the dissolution of quartz in a magmatic melt, since the experimental dissolution front is flat [e.g., *Acosta-Vigil et al.*, 2005]. Some of reentrants were partially or completely filled with fluid, raising the question of how the magma became bubbly at the storage depth before the eruption [*Befus and Manga*, 2019]. Flushing with CO_2 can saturate the magma with the H_2O-CO_2 fluid and make it bubbly. An alternative mechanism is slow fractional crystallization caused by cooling of the magma, when excess fluid is exsolved [*Wallace et al.*, 1995].

Pichavant et al. [2013] extended the study of *Yoshimura and Nakamura* [2010] by experimental modelling the degassing of a basaltic melt initially saturated with CO_2 and water at $P = 200\,\mathrm{MPa}$. They found that when the pressure is reduced to 25–50 MPa at the fixed rate at a sufficiently low bubble number density (large inter bubble distance), a high supersaturation of CO_2 develops in the melt, while the water content follows equilibrium solubility (Figure 9). As with flushing, CO_2 and H_2O are decoupled due to their contrasting diffusivities. The control of the inter-bubble distance on CO_2 equilibration is very similar to the condition of disequilibrium Cpx growth in the Ab-Di-H_2O system [*Simakin et al.*, 2020]. Non-equilibrium hopper morphology of the crystal rim develops during quenching, when inter-crystalline distances exceed 5–8 µm. At a number density of crystals above $8\text{–}10 \times 10^9\,\mathrm{cm}^{-3}$, the diffusion of SiO_2 (the slowest component) homogenizes the melt composition to close to equilibrium. The diffusion coefficient of SiO_2 is many orders of magnitude lower than that of CO_2, so the threshold bubble number density is about 10^4 times lower than that of crystals. In *Pichavant et al.* [2013] study, the threshold bubble number density is determined by the time scale of experiments equal to $\tau_{\mathrm{exp}} = \Delta P/(\mathrm{d}P/\mathrm{d}t) = 1000\text{–}4000\,\mathrm{s}$. The diffusion coefficient of CO_2 in basalt melt at $T = 1150\,°\mathrm{C}$ is $1.3 \times 10^{-7}\,\mathrm{cm}^2/\mathrm{s}$, and the homogenization time $\tau_{CO_2} = W^2/D_{CO_2}$. The condition $\tau_{exp} \ll \tau_{D_{CO_2}}$ (compare with Figure 8) requires the bubble volume number density $N \approx 1/(W/2)^3 \ll 1.4\text{–}12 \times 10^6\,\mathrm{cm}^{-3}$, which corresponds to the experimentally estimated $N < 10^6\,\mathrm{cm}^{-3}$.

Combined in Figure 10 are experimental data from our experiments, *Pichavant et al.* [2013] and *Yoshimura and Nakamura* [2010] demonstrate that the two types of dynamic dehydration differ significantly from the equilibrium predictions shown in Figure 1. As our scaling analysis showed, slower diffusion of CO_2 than H_2O may be important on realistic time scales for magma flushing. Our assumption about the same size of the spherical shell of the melt for all bubbles, used in numerical simulation, ignores the uneven distribution of bubbles in the melt volume and their possible escape. These effects are reflected in our data for run a21, where the composition point are scattered over a wide range of CO_2 and H_2O contents and do not follow a single trend.

All this makes it difficult to interpret the data on the content of CO_2 and H_2O in MIs. In general, the CO_2 flushing model can be supported by the presence of low (near zero) CO_2 and high H_2O points on the diagram, which may represent the melt composition before CO_2 influx. However, such compositions are rare, for example, in Figure 1 data for HRT MIs do not have distinct points of both low and high water with low CO_2. Almost CO_2 free and water saturated compositions can also be produced at a high degree of magma crystallization with an exsolved fluid accumulating CO_2 [*Wallace et al.*, 1995]. The interpretation of MI data is further complicated by the possible loss of water after entrainment. Taking into account the isotopic fractionation of fluid-mobile components between the fluid and the melt can be a decisive argument. A correlation between CO_2 concentration and δ^{11}B, δ^{7}Li, δ^{34}S is expected if these components are extracted from the melt by a CO_2-enriched fluid along with H_2O. If unequivocal arguments will be obtained in favor of the significance of flushing with carbonic fluid, a mechanical model of interaction can be developed, including the effects of crystallization, an increase in the volume of multiphase magma, and a probable heating caused by the recharge of the magma chamber with more primitive magma accompanying flushing.

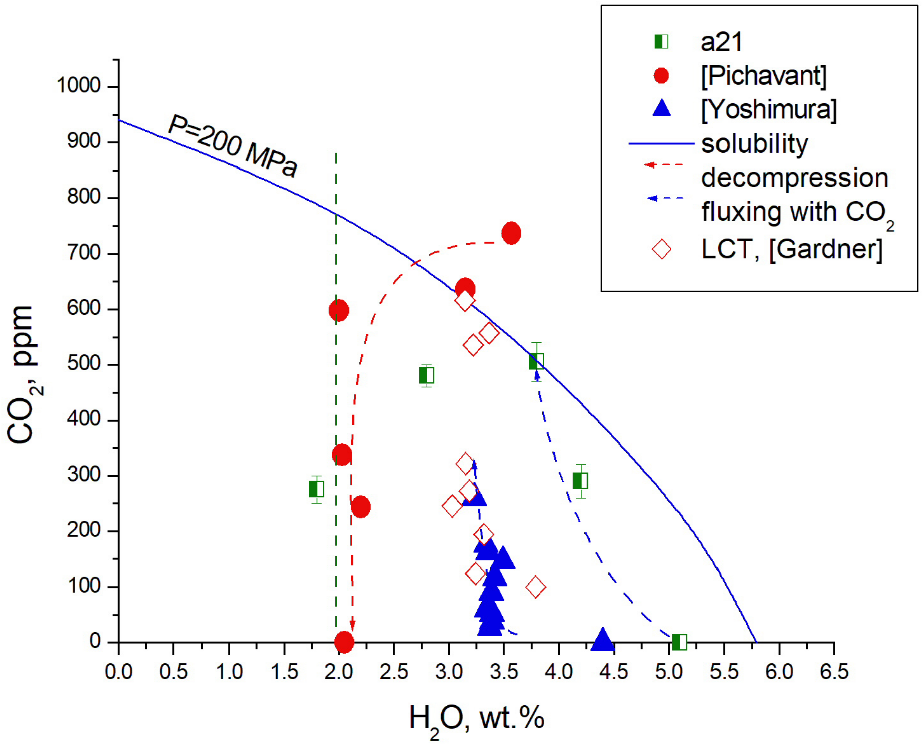

Figure 10. Diffusion-controlled trends in H_2O-CO_2 concentrations in the melt caused by CO_2 flushing and depressuration-induced vesiculation. The filled triangles display the profile distribution at the interface of the melt and CO_2 enriched fluid from [*Yoshimura and Nakamura*, 2010]. Partially filled squares refer to the experiment a21 with numerous CO_2 bubbles, the large data spread reflects uneven distribution of the bubbles in the melt with contrasting residence times. The vertical dahed line indicates the water content achieved with complete equilibration of the melt-fluid system without crystalllization. Filled circles correspond to the experiment on vesiculation during depressurization of a basaltic melt saturated with CO_2-H_2O fluid at $P = 200$ MPa from [*Pichavant et al.*, 2013].

Conclusions

1. Numerical modeling of the exchange of volatiles and the growth of a CO_2 bubble in a hydrous silicic melt is performed. It is demonstrated that water distribution between neighboring bubbles becomes uniform over a time equal to $\approx 0.14W^2/D_\mathrm{w}$, where W is an inter-bubble distance, D_w is water diffusion coefficient and occurs when the melt is still undesaturated with CO_2.
2. Experiments with albite melt with an initial water content of about 5 wt. % at $P = 200$ MPa and $T = 950\,°C$ showed that the initial content of CO_2 bubbles, with characteristic radii of tens of microns, reduces from to ~ 40 to 13 vol. % in 40 minutes due to the bubble escape. Flushing of the melt with mm-size CO_2 bubbles leads to uneven dehydration with a decrease in water content to 1.8–4.1 wt. %. The CO_2 concentration measured with µ-FTIR is 200–500 ppm, in general is below the saturation.
3. In a partially dehydrated melt rapid crystallization of albite with the release of volatiles is observed after 40 min, whereas the volume fraction of crystals increases to 70 vol. % in 4 hours. The estimated concentration of water in the residual melt approaches the maximum value of 2.5–2.8 wt. % close to the limit required for melt-crystal equilibrium under the experimental PT conditions.
4. Series of experiments on the exchange of volatiles between the CO_2 fluid and the hydrous albite melt through a discrete interface were performed at $T = 1020\,°C$ and $P = 200$ MPa. In these experiments, the linear scale of the diffusion process increased

to several millimeters. The measured content of water and CO_2 at the interface is 2 wt. % and 200 ppm, respectively, which significantly exceeds the value imposed by fluid-melt exchange. We explain this by the formation of a SiO_2 rich protective film on the contact due to the preferential dissolution of Na_2O and Al_2O_3 in the carbonic fluid. Diffusion profiles in glass were measured using EMPA (H_2O) and µ-FTIR (H_2O and CO_2). The diffusion coefficients of H_2O (1.1×10^{-6} cm^2/s) and CO_2 (1.5×10^{-7} cm^2/s) obtained by fit of these profiles agree with the published data.

5. Possible episodes of interaction (flushing) of CO_2 enriched fluid and hydrous silicic magma will produce melts with dissolved CO_2 and H_2O contents following a disequilibrium distinctive trend. Due to the slow diffusion mobility of CO_2, the melt will first be dehydrated and then enriched with CO_2, which might be reflected in the composition of melt inclusions in quartz.

Acknowledgements. Authors thank for invaluable contribution of A.N. Nekrasov in EMPA analyses of our experimental samples and G. V. Bondarenko for assistance in the Raman investigation of the bubbles. The authors are also grateful to R. E. Botcharnikov and anonymous reviewer for critical comments that clarify the presentation of the results and significantly improve the MS.

References

Acosta-Vigil, A., D. London, G. B. Morgan, and T. A. Dewers (2005), Dissolution of Quartz, Albite, and Orthoclase in H_2O-Saturated Haplogranitic Melt at 800 °C and 200 MPa: Diffusive Transport Properties of Granitic Melts at Crustal Anatectic Conditions, *Journal of Petrology*, *47*(2), 231–254, https://doi.org/10.1093/petrology/egi073.

Barry, P. H., D. R. Hilton, E. Föri, S. A. Halldórsson, and K. Grönvold (2014), Carbon isotope and abundance systematics of Icelandic geothermal gases, fluids and subglacial basalts with implications for mantle plume-related CO_2 fluxes, *Geochimica et Cosmochimica Acta*, *134*, 74–99, https://doi.org/10.1016/j.gca.2014.02.038.

Befus, K. S., and J. E. Gardner (2016), Magma storage and evolution of the most recent effusive and explosive eruptions from Yellowstone Caldera, *Contributions to Mineralogy and Petrology*, *171*(4), https://doi.org/10.1007/s00410-016-1244-x.

Befus, K. S., and M. Manga (2019), Supereruption quartz crystals and the hollow reentrants, *Geology*, *47*(8), 710–714, https://doi.org/10.1130/G46275.1.

Behrens, H. (2010), Ar, CO_2 and H_2O diffusion in silica glasses at 2 kbar pressure, *Chemical Geology*, *272*(1–4), 40–48, https://doi.org/10.1016/j.chemgeo.2010.02.001.

Behrens, H., C. Romano, M. Nowak, F. Holtz, and D. B. Dingwell (1996), Near-infrared spectroscopic determination of water species in glasses of the system MAlSi3O8 (M = Li, Na, K): an interlaboratory study, *Chemical Geology*, *128*(1–4), 41–63, https://doi.org/10.1016/0009-2541(95)00162-x.

Berkesi, M., T. Guzmics, C. Szabó, J. Dubessy, R. J. Bodnar, and other (2012), The role of CO_2-rich fluids in trace element transport and metasomatism in the lithospheric mantle beneath the Central Pannonian Basin, Hungary, based on fluid inclusions in mantle xenoliths, *Earth and Planetary Science Letters*, *331–332*, 8–20, https://doi.org/10.1016/j.epsl.2012.03.012.

Botcharnikov, R., M. Freise, F. Holtz, and H. Behrens (2005), Solubility of C-O-H mixtures in natural melts: new experimental data and application range of recent models, *Annals of Geophysics*, *48*(4/5), 633–646.

Caricchi, L., T. E. Sheldrake, and J. Blundy (2018), Modulation of magmatic processes by CO_2 flushing, *Earth and Planetary Science Letters*, *491*, 160–171, https://doi.org/10.1016/j.epsl.2018.03.042.

Cheng, A. H., M. A. Golberg, E. J. Kansa, and G. Zammito (2003), Exponential Convergence and H-C Multiquadric Collocation Method for Partial Differential Equations, *Numerical Methods for Partial Differential Equations*, *19*(5), 571–594, https://doi.org/10.1002/num.10062.

Cichy, S. B., R. E. Botcharnikov, F. Holtz, and H. Behrens (2010), Vesiculation and Microlite Crystallization Induced by Decompression: a Case Study of the 1991–1995 Mt Unzen Eruption (Japan), *Journal of Petrology*, *52*(7–8), 1469–1492, https://doi.org/10.1093/petrology/egq072.

Coenen, K., F. Gallucci, B. Mezari, E. Hensen, and M. van Sint Annaland (2018), An in-situ IR study on the adsorption of CO_2 and H_2O on hydrotalcites, *Journal of CO_2 Utilization*, *24*, 228–239, https://doi.org/10.1016/j.jcou.2018.01.008.

Couch, S. (2003), The Kinetics of Degassing-Induced Crystallization at Soufriere Hills Volcano, Montserrat, *Journal of Petrology*, *44*(8), 1477–1502, https://doi.org/10.1093/petrology/44.8.1477.

Coumans, J. P., E. W. Llewellin, F. B. Wadsworth, M. C. S. Humphreys, S. A. Mathias, B. M. Yelverton, and J. E. Gardner (2020), An experimentally validated numerical model for bubble growth in magma, *Journal of Volcanology and Geothermal Research*, *402*, 107,002, https://doi.org/10.1016/j.jvolgeores.2020.107002.

Dallai, L., R. Cioni, C. Boschi, and C. D'Oriano (2011), Carbonate-derived CO_2 purging magma at depth: Influence on the eruptive activity of Somma-Vesuvius, Italy, *Earth and Planetary Science Letters*, *310*(1–2), 84–95, https://doi.org/10.1016/j.epsl.2011.07.013.

Frezzotti, M.-L., and J. L. R. Touret (2014), CO_2, carbonate-rich melts, and brines in the mantle, *Geoscience Frontiers*, *5*(5), 697–710, https://doi.org/10.1016/j.gsf.2014.03.014.

Frezzotti, M. L., A. Peccerillo, and G. Panza (2010), Earth's CO_2 degassing in Italy, *Journal of the Virtual Explorer*, *36*, https://doi.org/10.3809/jvirtex.2010.00227.

Gurenko, A. A. (2021), Origin of sulphur in relation to silicate-sulphide immiscibility in Tolbachik primitive arc magma (Kamchatka, Russia): Insights from sulphur and boron isotopes, *Chemical Geology*, *576*, 120,244, https://doi.org/10.1016/j.chemgeo.2021.120244.

Hidas, K., T. Guzmics, C. Szabó, I. Kovács, R. J. Bodnar, and other (2010), Coexisting silicate melt inclusions and H_2O-bearing, CO_2-rich fluid inclusions in mantle peridotite xenoliths from the Carpathian-Pannonian region (central Hungary), *Chemical Geology*, *274*(1–2), 1–18, https://doi.org/10.1016/j.chemgeo.2010.03.004.

Holland, T. (2001), Calculation of Phase Relations Involving Haplogranitic Melts Using an Internally Consistent Thermodynamic Dataset, *Journal of Petrology*, *42*(4), 673–683, https://doi.org/10.1093/petrology/42.4.673.

Hui, H., and Y. Zhang (2007), Toward a general viscosity equation for natural anhydrous and hydrous silicate melts, *Geochimica et Cosmochimica Acta*, *71*(2), 403–416, https://doi.org/10.1016/j.gca.2006.09.003.

Kerrick, D. M., and G. K. Jacobs (1981), A modified Redlich-Kwong equation for H_2O, CO_2 , and $H_2O–CO_2$ mixtures at elevated pressures and temperatures, *American Journal of Science*, *281*, 735–767.

King, P. L., and J. R. Holloway (2002), CO_2 solubility and speciation in intermediate (andesitic) melts: the role of H_2O and composition, *Geochimica et Cosmochimica Acta*, *66*(9), 1627–1640, https://doi.org/10.1016/S0016-7037(01)00872-9.

Konschak, A., and H. Keppler (2014), The speciation of carbon dioxide in silicate melts, *Contributions to Mineralogy and Petrology*, *167*(5), https://doi.org/10.1007/s00410-014-0998-2.

Longpré, M.-A., J. Stix, A. Klügel, and N. Shimizu (2017), Mantle to surface degassing of carbon- and sulphur-rich alkaline magma at El Hierro, Canary Islands, *Earth and Planetary Science Letters*, *460*, 268–280, https://doi.org/10.1016/j.epsl.2016.11.043.

Lowenstern, J. B., and S. Hurwitz (2008), Monitoring a Supervolcano in Repose: Heat and Volatile Flux at the Yellowstone Caldera, *Elements*, *4*(1), 35–40, https://doi.org/10.2113/gselements.4.1.35.

Lyakhovsky, V., S. Hurwitz, and O. Navon (1996), Bubble growth in rhyolitic melts: experimental and numerical investigation, *Bulletin of Volcanology*, *58*(1), 19–32, https://doi.org/10.1007/s004450050122.

Mollo, S., M. Gaeta, C. Freda, T. D. Rocco, V. Misiti, and P. Scarlato (2010), Carbonate assimilation in magmas: A reappraisal based on experimental petrology, *Lithos*, *114*(3–4), 503–514, https://doi.org/10.1016/j.lithos.2009.10.013.

Myers, M. L., P. J. Wallace, C. J. N. Wilson, B. K. Morter, and E. J. Swallow (2016), Prolonged ascent and episodic venting of discrete magma batches at the onset of the Huckleberry Ridge supereruption, Yellowstone, *Earth and Planetary Science Letters*, *451*, 285–297, https://doi.org/10.1016/j.epsl.2016.07.023.

Narine, S. S., K. L. Humphrey, and L. Bouzidi (2006), Modification of the Avrami model for application to the kinetics of the melt crystallization of lipids, *Journal of the American Oil Chemists' Society*, *83*(11), 913–921, https://doi.org/10.1007/s11746-006-5046-6.

Navon, O., A. Chekhmir, and V. Lyakhovsky (1998), Bubble growth in highly viscous melts: theory, experiments, and autoexplosivity of dome lavas, *Earth and Planetary Science Letters*, *160*(3–4), 763–776, https://doi.org/10.1016/s0012-821x(98)00126-5.

Neukampf, J., O. Laurent, P. Tollan, A.-S. Bouvier, T. Magna, and other (2022), Degassing from magma reservoir to eruption in silicic systems: The Li elemental and isotopic record from rhyolitic melt inclusions and host quartz in a Yellowstone rhyolite, *Geochimica et Cosmochimica Acta*, *326*, 56–76, https://doi.org/10.1016/j.gca.2022.03.037.

Newman, S., and J. B. Lowenstern (2002), VolatileCalc: a silicate melt-H_2O–CO_2 solution model written in Visual Basic for excel, *Computers & Geosciences*, *28*(5), 597–604, https://doi.org/10.1016/s0098-3004(01)00081-4.

Pichavant, M., I. Di Carlo, S. G. Rotolo, B. Scaillet, A. Burgisser, N. Le Gall, and C. Martel (2013), Generation of CO_2-rich melts during basalt magma ascent and degassing, *Contributions to Mineralogy and Petrology*, *166*(2), 545–561, https://doi.org/10.1007/s00410-013-0890-5.

Ruefer, A. C., K. S. Befus, J. O. Thompson, and B. J. Andrews (2021), Implications of Multiple Disequilibrium Textures in Quartz-Hosted Embayments, *Frontiers in Earth Science*, *9*, https://doi.org/10.3389/feart.2021.742895.

Rusiecka, M. K., and D. R. Baker (2021), Growth and textural evolution during crystallization of quartz and feldspar in hydrous, rhyolitic melt, *Contributions to Mineralogy and Petrology*, *176*(7), https://doi.org/10.1007/s00410-021-01809-1.

Simakin, A., H. Schmeling, and V. Trubitsyn (1997), Convection in melts due to sedimentary crystal flux from above, *Physics of the Earth and Planetary Interiors*, *102*(3–4), 185–200, https://doi.org/10.1016/S0031-9201(97)00010-1.

Simakin, A. G., and I. N. Bindeman (2022), Convective Melting and Water Behavior around Magmatic-Hydrothermal Transition: Numerical Modeling with Application to Krafla Volcano, Iceland, *Journal of Petrology*, *63*(8), https://doi.org/10.1093/petrology/egac074.

Simakin, A. G., and V. Y. Chevychelov (1995), Experimental studies of feldspar crystallization of granite melts of varied water content, *Geokhimiya*, (2), 216–237.

Simakin, A. G., and A. Ghassemi (2018), Mechanics of Magma Chamber with the Implication of the Effect of CO_2 Fluxing, in *Volcanoes - Geological and Geophysical Setting, Theoretical Aspects and Numerical Modeling, Applications to Industry and Their Impact on the Human Health*, chap. 9, pp. 175–207, InTech, https://doi.org/10.5772/intechopen.71655.

Simakin, A. G., P. Armienti, and M. B. Epelbaum (1999), Coupled degassing and crystallization: experimental study at continuous pressure drop, with application to volcanic bombs, *Bulletin of Volcanology*, *61*(5), 275–287, https://doi.org/10.1007/s004450050297.

Simakin, A. G., T. P. Salova, and G. V. Bondarenko (2012), Experimental study of magmatic melt oxidation by CO_2, *Petrology*, *20*(7), 593–606, https://doi.org/10.1134/S0869591112070053.

Simakin, A. G., V. N. Devyatova, and A. N. Nekrasov (2020), *Crystallization of Cpx in the Ab-Di System Under the Oscillating Temperature: Contrast Dynamic Modes at Different Periods of Oscillation*, pp. 97–120, Springer International Publishing, https://doi.org/10.1007/978-3-030-42859-4_5.

Stolper, E. M., G. Fine, T. Johnson, and S. Newman (1987), Solubility of carbon dioxide in albitic melt, *American Mineralogist*, (72), 1071–1085.

Swanson, S. E., and P. M. Fenn (1986), Quartz crystallization in igneous rocks, *American Mineralogist*, *71*(3-4), 331–342.

Wallace, P. J., A. T. Anderson, and A. M. Davis (1995), Quantification of pre-eruptive exsolved gas contents in silicic magmas, *Nature*, *377*(6550), 612–616, https://doi.org/10.1038/377612a0.

Wang, X., I.-M. Chou, W. Hu, R. C. Burruss, Q. Sun, and Y. Song (2011), Raman spectroscopic measurements of CO_2 density: Experimental calibration with high-pressure optical cell (HPOC) and fused silica capillary capsule (FSCC) with application to fluid inclusion observations, *Geochimica et Cosmochimica Acta*, *75*(14), 4080–4093, https://doi.org/10.1016/j.gca.2011.04.028.

Werner, C., and S. Brantley (2003), CO_2 emissions from the Yellowstone volcanic system, *Geochemistry, Geophysics, Geosystems*, *4*(7), https://doi.org/10.1029/2002gc000473.

Yamamoto, J., and H. Kagi (2006), Extended Micro-Raman Densimeter for CO_2 Applicable to Mantle-originated Fluid Inclusions, *Chemistry Letters*, *35*(6), 610–611, https://doi.org/10.1246/cl.2006.610.

Yinnon, H., and D. R. Uhlmann (1983), Applications of thermoanalytical techniques to the study of crystallization kinetics in glass-forming liquids, part I: Theory, *Journal of Non-Crystalline Solids*, *54*(3), 253–275, https://doi.org/10.1016/0022-3093(83)90069-8.

Yoshimura, S., and M. Nakamura (2010), Chemically driven growth and resorption of bubbles in a multivolatile magmatic system, *Chemical Geology*, *276*, 18–28.

Zanotto, E. D., and D. R. Cassar (2017), The microscopic origin of the extreme glass-forming ability of Albite and B2O3, *Scientific Reports*, *7*(1), https://doi.org/10.1038/srep43022.

Zelenski, M., A. Simakin, Y. Taran, V. S. Kamenetsky, and N. Malik (2021), Partitioning of elements between high-temperature, low-density aqueous fluid and silicate melt as derived from volcanic gas geochemistry, *Geochimica et Cosmochimica Acta*, *295*, 112–134, https://doi.org/10.1016/j.gca.2020.12.011.

Zelenski, M., V. S. Kamenetsky, N. Nekrylov, and A. Kontonikas-Charos (2022), High Sulfur in Primitive Arc Magmas, Its Origin and Implications, *Minerals*, *12*(1), 37, https://doi.org/10.3390/min12010037.

Zhang, Y., and H. Ni (2010), Diffusion of H, C, and O Components in Silicate Melts, *Reviews in Mineralogy and Geochemistry*, *72*(1), 171–225, https://doi.org/10.2138/rmg.2010.72.5.